Monatshefte für Chemie 133, 837–848 (2002)

Monatshefte für Chemie
Chemical Monthly

Characterization of Nanocomposite Coatings in the System Ti–B–N by Analytical Electron Microscopy and X-Ray Photoelectron Spectroscopy

Andreas Gupper[1], **Asunción Fernández**[2], **Christina Fernández-Ramos**[2], **Ferdinand Hofer**[1,*], **Christian Mitterer**[3], and **Peter Warbichler**[1]

[1] Forschungsinstitut für Elektronenmikroskopie, Technische Universität Graz, and Zentrum für Elektronenmikroskopie Graz, A-8010 Graz, Austria
[2] Instituto de Ciencia de Materiales de Sevilla, Centro de Investigaciones Científicas Isla de la Cartuja, E-41092 Sevilla, Spain
[3] Institut für Metallkunde und Werkstoffprüfung, Montanuniversität Leoben, A-8700 Leoben, Austria

Summary. Superhard nanocomposite coatings of different composition in the *quasi*-binary system $TiN–TiB_2$ were deposited onto stainless steel sheets by means of unbalanced DC magnetron co-sputtering using segmented TiN/TiB_2 targets. The chemistry and microstructure of a $TiB_{0.6}N_{0.7}$ coating was investigated using X-ray and electron diffraction, photoelectron spectroscopy, energy-filtering transmission electron microscopy, and electron energy-loss spectrometry. High resolution elemental mapping of the elements Ti, B, N, and O with energy-filtering TEM reveals a homogeneous distribution on the nanometer scale. X-Ray and electron diffraction exhibit only TiN crystallites of nanometer size, but no information on the boron-rich phase. The near-edge fine structures of the B*K* and N*K* ionization edges in the EELS spectra of the Ti–B–N coatings were used to derive information on the phases by comparing the edges with those of reference compounds. It was found that the TiN nanocrystals occur together with TiO_x particles; the grains are embedded in a strongly disordered or *quasi*-amorphous matrix consisting mainly of TiB_2 particles and, near the steel substrate, also boron oxide (B_2O_3).

Keywords. Nanostructures; Electron microscopy; EELS; EFTEM; XPS; XRD.

Introduction

Nanocomposite coating materials have recently attracted increasing interest due to the possibility of the synthesis of materials with unique properties, *e.g.* superhardness [1], combined high hardness and toughness [2], or hardness and low friction [3]. There is an increasing number of nanocomposite wear-resistant coating material systems, such as $TiN–Si_3N_4$ [1, 4], Ti–B–N [5], and $Ti–B–N–MoS_2$ [6].

* Corresponding author. E-mail: ferdinand.hofer@tugraz.at

In order to understand the origin of the exceptional properties of these materials and possible trends it is imperative to have a good comprehension of the multiphase composition and microstructure. The lack of knowledge in this field stems not only from the poorly understood micromechanical mechanisms, but also from the difficulty of characterizing these nanocrystalline materials, the resolution limits of analytical techniques often being not sufficient.

Previously, characterization of nanocomposite coatings has mainly been performed by X-ray photoelectron spectroscopy (XPS), *Auger* electron spectroscopy (AES), X-ray diffraction (XRD), electron-probe microanalysis (EPMA), and extended X-ray absorption fine structure analysis (EXAFS) [7]. However, since these techniques are not always sufficient for studying nanocomposite coatings, it is necessary to obtain structural information beyond that available from conventional techniques. In this paper, we apply modern techniques of transmission electron microscopy (TEM) as already demonstrated in previous investigations [8, 9]. We extend these investigations by means of a combination of an electron microscope with an imaging energy filter to perform energy-filtered imaging (EFTEM) and electron energy-loss spectroscopy (EELS). The aim of the present study is to gain chemical and structural information on the phases and to investigate the distribution of the elements with the highest possible lateral resolution. One major point of the present study is to apply the electron energy-loss near edge fine structures technique (ELNES) which has proved fruitful in studying boron and nitrogen containing compounds due to the information provided about bonding and nearest neighbours [10, 11].

Results and Discussion

In order to study nanocomposites consisting of TiB_2 and TiN, the elemental coating composition was adjusted to the *quasi*-binary tie line between the individual compounds in the system Ti–B–N [9]. The results of XRD analysis for different chemical compositions are summarized in Fig. 1. The TiB_2-based layer exhibited the well-known strong (001)-preferred orientation of the hcp TiB_2 phase [5], whereas in TiN films fcc TiN with a random orientation was formed [16]. The gracing angle traces for Ti–B–N samples did not reveal well-defined diffraction patterns as for the TiB_2- or TiN-based layers. It is already well known that the very small grain size in nanophase materials gives their diffraction pattern the appearance of an amorphous material [2, 17]. This can be also observed for the Ti–B–N samples, where the X-ray peaks are considerably broadened, thus indicating very small crystal grains in the range of some nanometers. However, it is only possible to identify the X-ray lines due to TiN crystallites. Additionally, a gradual shift of the line positions of TiN to lower angles can be observed, thus indicating a widening of the TiN lattice.

X-Ray photoelectron spectroscopy lead to some valuable information concerning the surface composition. It brought clear evidence for the existence of more than one boron and nitrogen containing compound. The B1s, N1s, and O1s spectra of one sample before and after sputtering used for interpretation are shown in Fig. 2. In the B1s spectra, two large peaks at 186.7 and 191.2 eV are visible which were assigned to TiB_2 and B_2O_3, respectively. Table 1 summarizes the binding

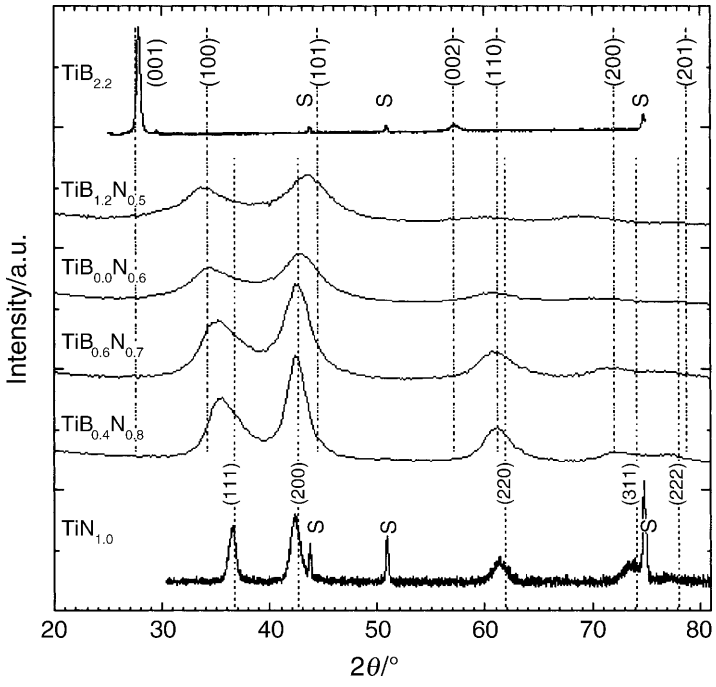

Fig. 1. XRD patterns of Ti–B–N coatings of different compositions on steel substrates

energies for possible boron containing compounds and the corresponding references. The peak for the latter component in the boron spectra appears at relatively low binding energy as compared to the literature (193.1 eV) [18]. This could be due to a deficiency of oxygen or the incorporation of titanium. Furthermore, it is obvious that there is no elemental boron present at the surface, as no signal was observed at 186.5 eV [19]. The N1s spectra show more then one signal with TiN as the main component at about 396 eV. The peak at higher binding energy disappears during the sputtering process, probably because of the removal of a nitrogen containing surface contamination. The oxygen spectrum displays two main contributions. The component at higher binding energies indicates the presence of water adsorbed onto the surface which is removed after ion sputtering. The component at lower binding energies results from the incorporation of oxygen inside the film due to the high avidity of Ti and B for this element. The existence of B_2O_3 has been already discussed, and oxidized titanium can also be seen in the Ti2p XPS spectra (not shown). The films are not only oxidized at the surface, but they present a certain level of bulk oxidation which remains after sputtering (Fig. 2) as is confirmed by quantitative EELS analysis. The quantification of the XPS spectrum for the $TiB_{0.6}N_{0.7}$ sample is shown in Table 2. The oxygen content is rather high (about 46 at%) which may be explained by surface oxidation of the nanocomposite layers, the XPS spectrum being recorded at the surface of the layer.

In case of the single-phase TiN coatings, the SEM investigation of fracture cross-sections showed the well-known columnar structures, but the layers with increasing boron content showed dense, featureless glass-like structures [8–10]. The TEM bright field image of a Ti–B–N nanocomposite cross-section foil

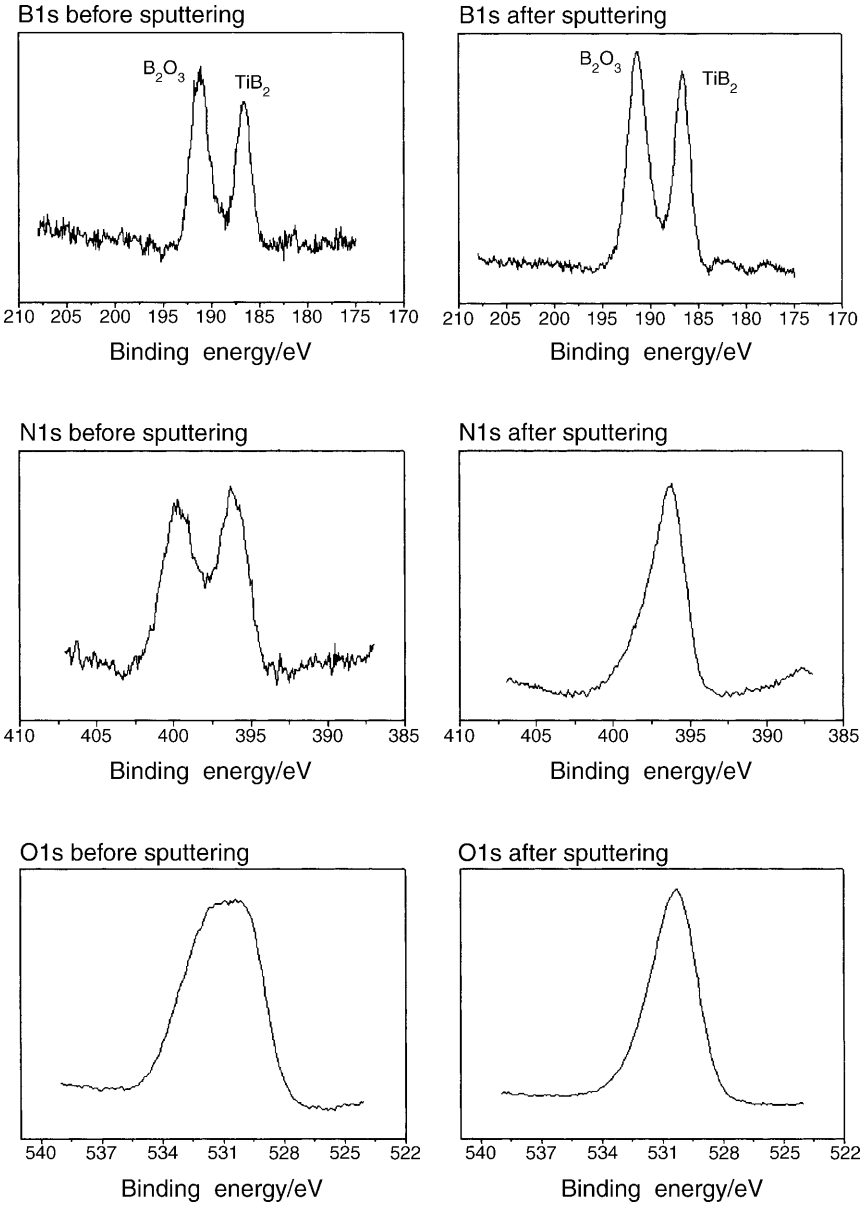

Fig. 2. XPS spectra of a coating with the composition $TiB_{0.6}N_{0.7}$; B1s, N1s, and O1s before and after sputtering

Table 1. Binding energies of some boron containing compounds

Compound	B_2O_3	BN	TiB_2	B
Binding energy/eV	193,1	190,5	187,5	186,5
Reference	[15]	[15]	[15]	[16]

Table 2. Results of the quantification of the XPS and EELS spectra of $TiB_{0.6}N_{0.7}$ (in at%) and the phases identified by different analytical techniques (XPS, XRD, ED, EELS, ELNES)

	Location	Ti	B	N	O	Compounds
XPS	Surface	25.0	21.0	7.0	46.0	
EELS	Near surface	27.8	20.6	32.2	19.4	TiB_2, TiN, TiO, C
	Middle	31.5	19.8	24.4	24.3	TiB_2, TiN, TiO, C
	Near substrate	26.0	12.0	18.4	43.6	TiB_2, TiN, B_2O_3, TiO, C

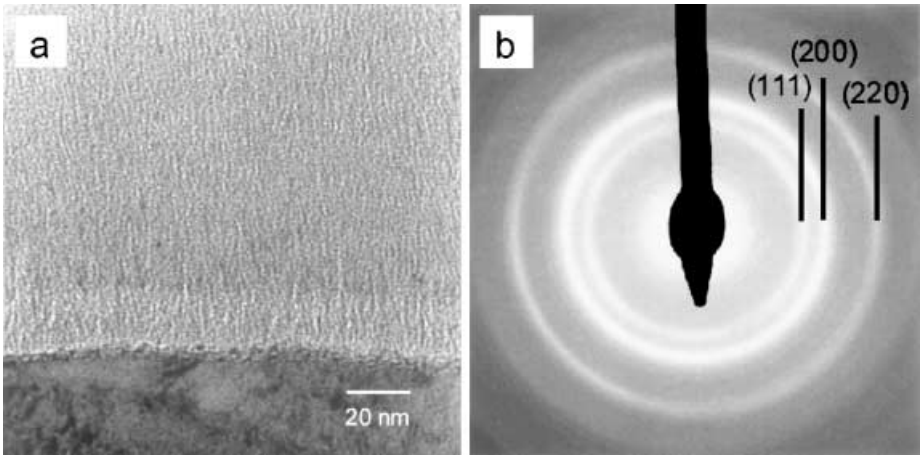

Fig. 3. TEM cross-section of a coating with the composition $TiB_{0.6}N_{0.7}$ deposited onto an austenitic stainless steel substrate; a) TEM bright field image, b) corresponding selected area diffraction pattern indicating TiN crystallites of nanometer diameter

(Fig. 3a) revealed crystallites of approximately 3 to 5 nm. With the deposition parameters used, we observed no pronounced influence on the grain size. Contrary to the well-known competitive growth and grain coarsening following nucleation and coalescence, the crystallite size does not vary significantly with increasing film thickness. The rings of the selected electron diffraction pattern shown in Fig. 3b belong to the (111), (200), and (220) reflections of the TiN phase. They are in good agreement with the XRD results obtained for the same film composition. Similar to XRD results, the measured d values are up to 6% higher than the values found for TiN. This may be explained by the incorporation of boron in the TiN phase or by a disordered structure and hence high residual stresses. However, both diffraction methods showed no sign of the TiB_2 phase, which raises the question how the boron-rich phase is distributed within the layer.

In order to investigate the phase distribution, we recorded EFTEM elemental distribution maps of the interface region near the steel substrate. Figure 4 shows the elemental maps of titanium, nitrogen, boron, and oxygen. The only features distinguishable are a thin oxygen-enriched zone at the substrate/coating interface which is probably due to the natural oxide layer on the steel surface and a thicker zone close to this interface with increased boron and nitrogen content [8].

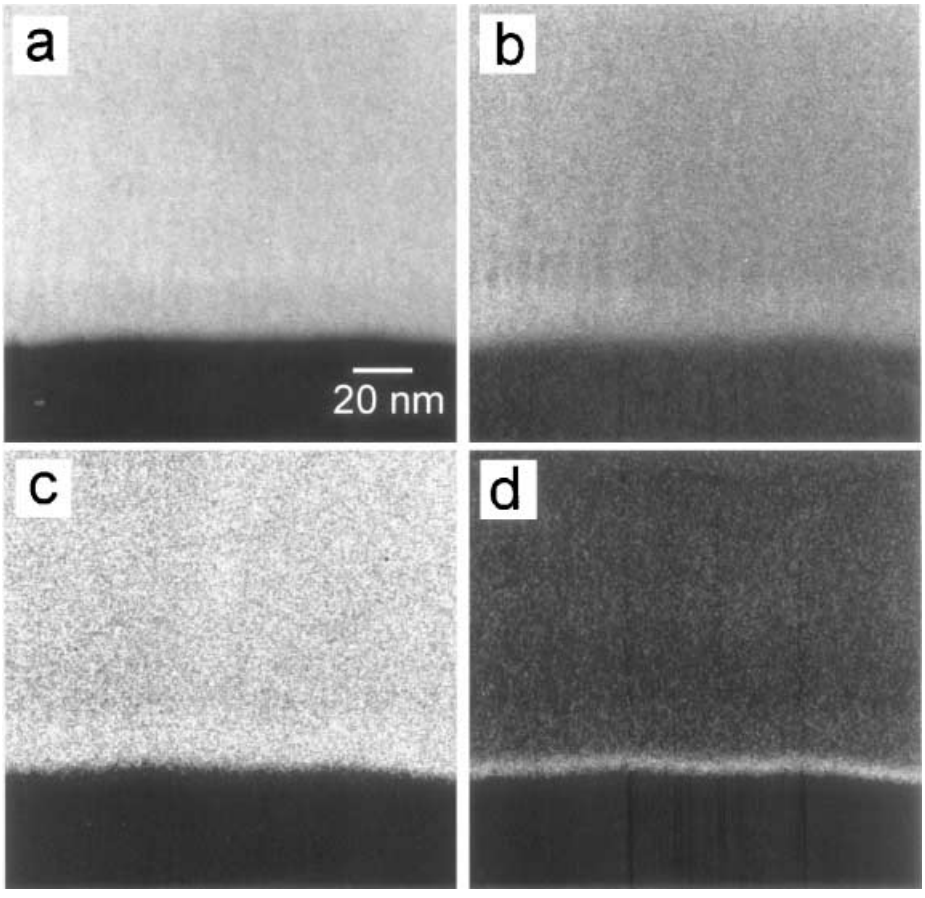

Fig. 4. EFTEM elemental maps of a coating with the average composition $TiB_{0.6}N_{0.7}$ near to the interface to the substrate; a) Ti$L_{2,3}$ jump ratio image, b) B*K* jump ratio image, c) N*K* jump ratio image, d) O*K* jump ratio image

Although EFTEM elemental mapping can be performed with a spatial resolution of about 1–2 nm, it is not possible to distinguish the phases present in this nanocrystalline sample. The origin of this drawback is that the TEM and EFTEM images are two-dimensional projections of three-dimensional samples. Since the specimen thickness of the ion-milled sample shown in Figs. 3 and 4 is about 30 nm and the crystals are smaller and randomly distributed, they cannot be seen in the projection. This principal limitation of EFTEM in the characterization of nanocrystalline materials has been often overlooked until now. However, in spite of the apparently homogeneous distribution of the boron and nitrogen elements in the films shown by EFTEM, the presence of two separated compounds, TiN and TiB_2, instead of a possible ternary Ti–B–N phase could be detected by the binding energy values of the corresponding XPS signals.

Nevertheless, in order to obtain more detailed information on the chemical phases of the Ti–B–N layers, we used advanced analytical techniques. In Fig. 5, EELS spectra collected for different positions on this cross-section are shown. It is evident that the coating contains not only boron, titanium, and nitrogen, but also oxygen and a small amount of carbon. Furthermore, the ionization edge intensities

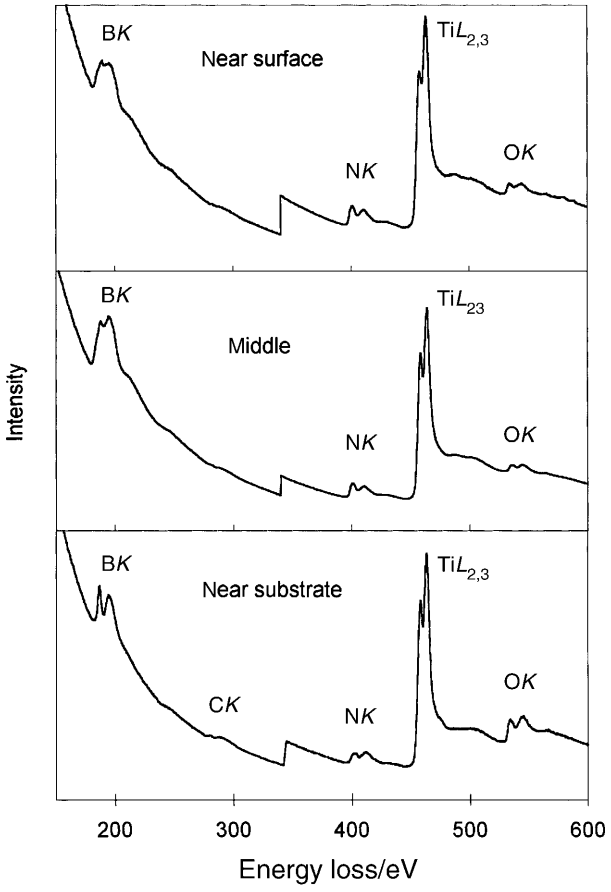

Fig. 5. EELS spectra of a coating with the average composition $TiB_{0.6}N_{0.7}$ (shown in Fig. 1) at different positions of the coating

vary due to concentration changes, *e.g.* the region near the substrate contains more oxygen but less boron, and the edge fine structures change between the different positions, thus suggesting that not only the elemental composition but also the chemical compounds vary. Particularly, the B*K* edges from different regions within the Ti–B–N layers gave a wide range of ELNES features. The spectra recorded near the steel interface exhibited similar features to those found in B_2O_3, where trigonally coordinated boron gives rise to a π^* peak at 193 eV and a σ^* peak at 204 eV [20], thus indicating that most of the boron is bound in the form of boron oxide (in the bright layer visible in the boron map, Fig. 4b). The B*K* edges recorded in the middle of the layer and near the surface showed features that are similar to the spectrum of titanium diboride (Fig. 6).

Quantification of the spectrum from the middle position gives 31.5 at% Ti, 19.8 at% B, 24.4 at% N, and 24.3 at% O; other quantification results are summarized in Table 2. The comparison of the XPS results with the EELS analysis of the surface position shows similar values for the titanium and boron concentrations, but different nitrogen and oxygen contents. This may be explained by oxidation of titanium nitride in the uppermost layers of the Ti–B–N nanocomposite, which are only probed by XPS, even after sputtering for some minutes.

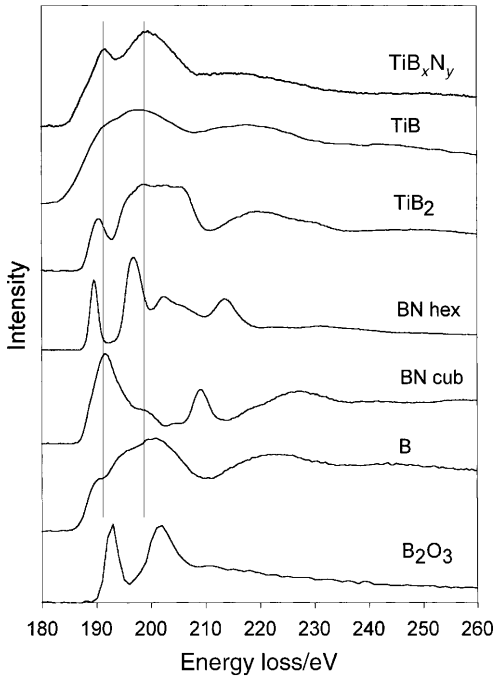

Fig. 6. Comparison of the B*K* edge of $TiB_{0.6}N_{0.7}$ from the middle position of the layer with B*K* edges from reference compounds (background below the ionization edges has been subtracted)

It is well known that the near-edge fine structures (ELNES) of the ionization edges reveal chemical bonding information and can be used as fingerprint information to identify chemical phases [10]. The main advantage of ELNES is its potential to examine changes in bonding with spatial resolution at the nanometer level and even approaching the level of interatomic changes [11].

For the elucidation of the chemical phases occurring in the Ti–B–N layers, we used the fingerprinting approach and compared the fine structures of the B*K*, N*K*, and O*K* edges recorded at the middle position of the layer ($TiB_{0.6}N_{0.7}$) with reference edges measured from TiN, TiB_2, B_2O_3, BN, and TiO_2 standards. Figure 6 shows the near-edge fine structure of the B*K* edges; the B*K* edge of the Ti–B–N coating is quite similar to the B*K* edge of TiB_2 and to some extent also to that of elemental boron and TiB. The B*K* edge of the Ti–B–N coating does not exhibit any ELNES feature of the BN compounds and of boron oxide, which means that these compounds do not occur in significant concentrations (<5 at%) in the coating. Furthermore, considering only the ELNES of the B*K* edge, the occurrence of elemental boron cannot be completely excluded, but XPS results showed that elemental boron does not occur in the Ti–B–N coating.

The main difference between the Ti–B–N coating and the TiB_2 standard is that the coating had been subjected to ion beam milling. However, it has been shown recently that ion milling does not cause a damage to nanocrystalline TiB_2 [21]. Since ELNES is strongly dependent on nearest neighbours and bonding, there is a possibility of impurity atoms causing the different spectra. A possible candidate is surely oxygen, which is measurable in all specimen regions. However, in the middle of the layer this oxygen is most probably correlated with the TiN phase,

because the ELNES of the O*K* edge in the Ti–B–N layers corresponds closely to that of TiO [22] which is isostructural to TiN (see Fig. 5).

Recently, it has been argued that changes in orientation are the main factor in producing a variation in the ELNES in TiB_2 [21]. There may be a number of reasons for this effect. Firstly, TiB_2 has a hexagonal structure like BN, but in contrast to BN it consists of monoelement layers, *i.e.* boron layers sandwiched between layers of titanium in the *a-b* plane. It therefore has anisotropic bonding within the whole structure, as the bonding within the layers will be different to any interlayer bonding. These differences are very directional, and hence it is perhaps not surprising that orientation effects are observed. However, in the polycrystalline fine-grained sample of Ti–B–N any ELNES differences will be averaged out.

In the B*K* edge of TiB_2 the feature at *ca.* 190 eV may be assigned to transitions to π^* states, whereas the broad peak at *ca.* 202 eV is associated with σ^* states as has been recently confirmed by multiple scattering calculations [21]. It is also important to mention that the B*K* edge is only similar to TiB_2 near the edge threshold, but shows significant changes for energy losses far above the edge threshold. This is a strong indication for a disordered structure which will be discussed below.

The above findings are confirmed for the N*K* edge (Fig. 7) which closely corresponds to that of crystalline TiN, but also shows a broadening of the edge fine structures far above the edge threshold. This means that essentially there is a cubic phase of TiN nanoparticles which are uniformly distributed in the coating layer. The N*K* edges of the BN compounds differ considerably, thus confirming that there is not much boron nitride in the sample.

The comparison of the B*K* and N*K* edges of Ti–B–N with the reference compounds TiB_2 and TiN shows that the features near the edge threshold are quite similar. This means that the nearest neighbour environment in Ti–B–N is similar to the references. However, with increasing energy losses (25–30 eV above edge threshold) a broadening of the edge features is observed. These resonances have been ascribed to the scattering from the first and second neighbour [23]. Using multiple scattering calculations of rock salt structured nitrides and oxides, *Kurata et al.* have identified the broad peak with scattering from the first non-metal shell [24]. Since the B*K* edge of TiB_2 in the Ti–B–N coating (Fig. 6) is more broadened than the N*K* edge in TiN (Fig. 7), we may expect that long-range order is lost to a higher degree in case of the TiB_2 particles. This is confirmed by X-ray and electron diffraction results, where it was not possible to detect crystalline TiB_2 in the Ti–B–N coatings. These results are in agreement with previous findings [7] where EXAFS spectroscopy of Ti–B–N coatings has shown that the second coordination shell of Ti atoms was reduced to an unreasonably low coordination number (less than two atoms), indicating high average disorder beyond the first boron or nitrogen coordination shell and no real long-range order [7].

Within the Ti–B–N system, separate elemental or binary phases are thermodynamically favoured during PVD growth of the coating. It is well known that the deposition rate and surface diffusion coefficient are two important parameters in determining the grain size of deposited monophase coatings [7]. In multiphase films, the grain size is further influenced by competitive growth between grains of different composition. For the Ti–B–N multiphase system, the grain size is limited to a few nanometers when two phases are present. If three or even five

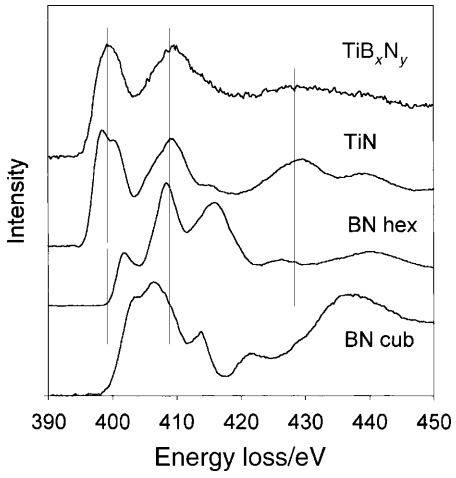

Fig. 7. Comparison of the N*K* edge of $TiB_{0.6}N_{0.7}$ from the middle position of the layer with N*K* edges from reference compounds (background below the ionization edges has been subtracted)

phases are formed, the grain size is progressively reduced to a point where well crystallized grains cannot be observed.

For a detailed information on the phases occurring in the magnetron sputtered Ti–B–N system, it is appropriate to summarize all experimental results which leads to the following model: There are two main phases TiN and TiB_2 all over the coating and at least two other phases such as B_2O_3, occurring mainly near the substrate and TiO in the middle of the layer. The well-crystallized TiN and TiO particles with an average diameter of several nanometers are embedded in a strongly disordered or *quasi*-amorphous phase consisting of TiB_2 and, near the steel substrate, also B_2O_3 (Table 2).

Finally, it has to be mentioned that techniques such as EXELFS or EXAFS have been successfully used to study bond lengths and coordination numbers in nanocrystalline materials (see Ref. [25]). However, these oscillations cannot be fully exploited, because they have to be collected from energy losses of 100 to 300 eV above the edge threshold. Since the B*K*, C*K*, or N*K* edges are only separated by *ca.* 100 eV and the N*K* edge overlaps with the Ti$L_{2,3}$ edge, the application of these techniques is very limited. Consequently, there is no choice to characterize multiphase nanocomposites by a combination of different methods such as electron and X-ray diffraction, photo electron spectroscopy, electron energy-loss spectroscopy, and near-edge fine structures techniques.

Conclusions

This experimental investigation has been concerned with understanding the microstructure and chemistry of nanocrystalline Ti–B–N layers using a combination of X-ray and electron diffraction, photoelectron spectroscopy, transmission electron microscopy, and electron energy-loss spectrometry. We can assume that the Ti–B–N nanocomposite coating consists mainly of TiN and TiO crystals with an average diameter of several nanometers which are embedded in a strongly disordered or *quasi*-amorphous phase consisting mainly of TiB_2 and, near the steel substrate, also

B_2O_3. This combined electron microscopic, XRD, and XPS study provides important information from which the physical and mechanical properties of the technological Ti–B–N materials can be understood and refined.

Experimental

Sample preparation

The unbalanced DC magnetron sputtering system has been described in detail elsewhere [12], and only essential features will be presented here. TiN and TiB_2 targets with diameters of 15 cm were cut in two halves, and one half of each was bonded onto a water-cooled backing plate. The target was positioned at a distance of 6 cm from the parallel-plate substrate assembly. The sputtering power density was maintained at approximately $2\,W \cdot cm^{-2}$. An external pair of *Helmholtz* coils was used to create a uniform axial magnetic field B_{ext}, which was adjusted between 0 and 80 G in the region between the target and the substrates to intensify the field from the outer magnetron pole. In this arrangement, coatings with a lateral gradient in the chemical composition and a typical thickness of 3 μm were deposited. As substrates, metallographically polished austenitic stainless steel (X 5 CrNi 18 10) was used. For deposition, the ion bombardment conditions were varied systematically, (ion energy resulting from bias voltages: self-bias to -100 V; ion-to-neutral flux ratio: 0.1 to 0.7).

Sample characterization

Chemical composition as well as structural and mechanical properties were investigated using electron-probe microanalysis (EPMA), scanning electron microscopy (SEM), and X-ray diffraction (XRD). The X-ray diffraction patterns were recorded with a Siemens D500 diffractometer in the *Bragg-Brentano* mode using CuK_α radiation. In addition, glancing angle XRD patterns were obtained using an unfiltered copper source at an incident angle of 1°.

XPS spectra were recorded using a VG-Escalab 210 spectrometer operating in the constant analyzer energy mode with a pass energy of 50 eV and normal detection angle. The binding energy reference was taken as the C1s peak of the carbon contamination of the samples at 284.6 eV. The X-ray source for all measurements was MgK_α (1253.6 eV). All samples were measured without surface treatment and after sputtering for 3 min with Ar^+ ions at 3 kV in the prechamber (5×10^{-6} mbar). In addition to a general spectrum over the whole energy range, zone spectra of B1s, C1s, N1s, O1s, and Ti2p with higher resolution were recorded.

TEM specimens were prepared by cross-sectioning the coatings and ion milling. The investigation was performed with a Philips CM20 TEM/STEM with an LaB_6 cathode operating at 200 kV and equipped with an energy filter (Gatan Imaging Filter, GIF) [13]. All images and EFTEM elemental maps were recorded with the slow-scan CCD camera of the GIF [14].

The spectra for the ELNES studies were acquired in the TEM image mode using a probe half angle of 1.5 mrad and a collection half angle of 7.6 mrad; a spectrometer dispersion of 0.2 eV per channel was used. The images and spectra recorded with the slow-scan CCD camera were corrected for dark current and gain variations. Although the specimens were thinner than the mean free path of inelastic scattering, the ionization edges were corrected for multiple scattering using a logarithmic *Fourier* deconvolution procedure [15]. The background below the ionization edges was subtracted using an $A \cdot E^{-r}$ model.

Acknowledgements

We gratefully acknowledge financial support by the SFB '*Elektroaktive Stoffe*' and the COST program 523 '*Nanostructured materials*'.

References

[1] Veprek S, Reiprich S (1995) Thin Solid Films **268**: 64
[2] Musil J, Vlcek J (1998) Mater Chem Phys **54**: 116
[3] Mollart TP, Baker M, Haupt J, Steiner A, Hammer P, Gissler W (1998) Surf Coat Technol **108/109**: 345
[4] Veprek S, Haussmann M, Reiprich S, Li S, Dian J (1996) Surf Coat Technol **86/87**: 394
[5] Mitterer C, Rauter M, Rödhammer P (1990) Surf Coat Technol **41**: 351
[6] Gilmore J, Baker MA, Gibson PN, Gissler W, Stoiber M, Losbichler P, Mitterer C (1998) Surf Coat Technol **108/109**: 345
[7] Baker MA, Mollart TP, Gibson PN, Gissler W (1997) J Vac Sci Technol **A15**(2): 284
[8] Mitterer C, Losbichler P, Hofer F, Warbichler P (1998) Vacuum **50**: 313
[9] Mitterer C, Mayrhofer PH, Beschliesser M, Losbichler P, Warbichler P, Hofer F, Gibson PN, Gissler W, Hruby H, Musil J, Vlcek J (1999) Surf Coat Technol **120/121**: 405
[10] Hofer F, Golob P (1987) Ultramicroscopy **21**: 379
[11] Keast VJ, Scott AJ, Brydson R, Williams DB, Bruley J (2001) J Microscopy **203**: 135
[12] Losbichler P, Mitterer C, Gibson PN, Gissler W, Hofer F, Warbichler P (1997) Surf Coat Technol **94/95**: 289
[13] Krivanek OL, Gubbens AJ, Dellby N, Meyer C (1992) Microsc Microanal Microstruct **3**: 187
[14] Hofer F, Warbichler P, Grogger W (1995) Ultramicroscopy **59**: 15
[15] Egerton RF (1996) Electron Energy-loss Spectroscopy in the Electron Microscope. Plenum Press, New York London
[16] Losbichler P, Mitterer C (1997) Surf Coat Technol **97**: 567
[17] Zanchet D, Hall BD, Ugarte D (2000) X-ray Characterization of Nanoparticles. In: Wang ZL (ed) Characterization of Nanophase Materials. Wiley-VCH, Weinheim, p 13
[18] Briggs D, Seah MP (eds) (1990) Practical Surface Analysis, 2nd edn, vol 1: Auger and X-ray Photoelectron Spectroscopy. Wiley, Chichester
[19] Schreifels JA, Maybury PC, Swartz WE (1980) J Catal **75**: 373
[20] Brydson R, Sauer H, Engel W, Zeitler E (1991) Microsc Microanal Microstruct **2**: 159
[21] Davock HJ, Tatlock GJ, Brydson R, Lawson KJ, Nicholls JR (1997) Inst Conf Ser No 153. IOP Publ Ltd, Bristol, p 609
[22] Mitterbauer C, Hofer F, Kothleitner G (2001) Proc Dreiländertagung für Elektronenmikroskopie, Innsbruck, Austria, p 32
[23] Lytle FW, Greegor RB, Panson AJ (1988) Phys Rev **B37**: 1550
[24] Kurata H, Lefevre E, Colliex C, Brydson R (1993) Phys Rev **B47**: 13763
[25] Fernández A, Sánchez-López JC, Caballero A, Martin JM, Vacher B, Ponsonnet L (1998) J Microsc **191**: 212

Received October 4, 2001. Accepted (revised) January 10, 2002